Modelling and Simulation in Materials Science and Engineering 28 (2020) 015006 (31 pages)

Modified Embedded Atom Method Potential for High Temperature Crystal-Melt Properties of Ti-Ni Alloys and its Application to Phase Field Simulation of Solidification

Sepideh Kavousi[1], Brian R. Novak[1], Michael I. Baskes[2,3], Mohsen Asle Zaeem[4], and Dorel Moldovan[1,5*]

[1]*Department of Mechanical and Industrial Engineering, Louisiana State University, Baton Rouge, LA 70803, United States*

[2]*Office of Research and Economic Development, Mississippi State University, Mississippi State, MS 39762, USA*

[3]*Los Alamos National Lab, Los Alamos, NM 87545, USA*

[4]*Department of Mechanical Engineering, Colorado School of Mines, Golden, CO 80401, United States*

[5]*Center for Computation and Technology, Louisiana State University, Baton Rouge, LA 70803, United States*

ABSTRACT

We developed new interatomic potentials, based on the second nearest-neighbor modified embedded-atom method (2NN-MEAM) formalism, for Ti, Ni, and the binary Ti-Ni system. These potentials were fit to melting points, latent heats, the binary phase diagrams for the Ti rich and Ni rich regions, and the liquid phase enthalpy of mixing for binary alloys, therefore they are particularly suited for calculations of crystal-melt interface thermodynamic and transport properties. The accuracy of the potentials for pure Ti and pure Ni were tested against both 0 K and high temperature properties by comparing various properties obtained from experiments or density functional theory calculations including structural properties, elastic constants, point-defect properties, surface energies, temperatures and enthalpies of phase transformations, and diffusivity and viscosity in the liquid phase. The fitted binary potential for Ti-Ni was also tested against various non-fitted properties at 0 K and high temperatures including lattice parameters, formation energies of different intermetallic compounds, and the temperature dependence of liquid density at various concentrations. The crystal-melt interfacial free energies obtained from simulations based on the newly developed Ti-Ni potential, show that the BCC alloys tend to have smaller

anisotropy compared with FCC alloys which is consistent with the finding from the previous studies comparing single component BCC and FCC materials. Moreover, the interfacial free energy and its anisotropy for Ti-2 atom% Ni were also used to parameterize a 2D phase field model utilized in solidification simulations . The phase field simulation predictions of microstructure development during solidification are in good agreement with a geometric model for dendrite primary arm spacing.

KEYWORDS: molecular dynamics simulation, Ti-Ni alloy, phase diagram, high temperature, crystal-melt coexistence, crystal-melt interfacial free energy, phase field simulation, solidification

*Corresponding author: phone: 225-578-6488; e-mail: dmoldo1@lsu.edu

I. INTRODUCTION

Many analytical, experimental, and numerical studies have focused on investigation of microstructural characteristics of dendrites formation during solidification. The focus of these studies range from prediction of multiple dendrite morphology parameters, like primary and secondary arm spacing [1-3] to the anticipation columnar-equiaxed transitions [4, 5]. The primary dendritic arm spacing (PDAS) and secondary dendritic arm spacing (SDAS) are two important characteristics that yield valuable information on the segregation patterns and the distribution of precipitates between the dendritic arms which are known to have a strong effect on the mechanical properties [2]. The columnar to equiaxed transitions (CET) during solidification are very important in the manufacturing of single-crystal materials, such as Ni-based superalloy single crystals for use in gas turbine blades [6].One technique used to repair these blades is laser metal forming; a process in which the laser velocity and power should be chosen so that the final microstructure consists of single crystal, columnar dendrites grown from the melt-pool instead of polycrystalline equiaxed grains [4]. Phase field (PF) modeling is a powerful method used extensively to study PDAS and CET. The major limiting factor for quantitative prediction of the microstructure with PF modeling is that to obtain quantitative predictions it requires inputting accurate

crystal-melt (CM) interfacial properties such as free energy, kinetic coefficient, and their anisotropies, properties which are difficult to obtain from experiments.

Classical molecular dynamics (MD) simulations have the capability to yield detailed understanding of the kinetic processes that occur during solidification [7]. MD simulations are also well suited for obtaining the CM anisotropic interfacial properties, such as the kinetic coefficient [8, 9] and the interfacial free energy [10, 11], as well as providing insights into the microstructural pattern formation during solidification [12]. To obtain accurate results it is of great importance for the MD simulations to use reliable interatomic potentials in simulations of systems at CM coexistence.

In this study, we chose to investigate the Ni-Ti binary system for its relevance to Ni-based superalloys and to investigate CM interfacial properties and solidification of a bcc alloy (Ni solute in Ti). Given that the two main solutes used in Ni-based super alloys are Ti and Al, the development of a reliable Ni-Ti potential capable of predicting high-temperature equilibrium CM boundary compositions is as an important step towards the establishing of an interatomic potential which can be used in simulations of the solidification of Ni-based superalloys. Many studies show that crystal structure is one of the main characteristic determining CM anisotropy [13]. The number of investigations into the anisotropic interface energies in FCC (Cu-Ag [11] and Ni-Cu alloy[14]) and BCC alloys (Fe-Cr [15], where both the elements have BCC structure) is fairly limited. As such, in this study, we calculate the CM interfacial free energy for alloys in the Ti-rich part of the phase diagram and investigate the effect of addition of Ni solute atoms to the bcc Ti matrix.

Several interatomic potentials have been developed for the Ti-Ni binary systems. These include the Finnis-Sinclair (FS) potentials [16] by Lai and Liu [17] and Ren and Sehitoglu [18], the modified-FS potentials by Mutter and Nielaba [19] and Zhong et al. [20], the Gupta potential by Kexel et al. [21], the embedded-atom method (EAM) potential [22] by Farkas et al. [23], the EAM type potential, referred to as a long-range empirical potential (LREP), by Li et al. [24], the modified-EAM method (MEAM) potentials [25] by Ishida and Hiwatari [26] and Saitoh et al. [27], and the second nearest-neighbor (2NN)

MEAM potentials [28] by Ko et al. [29], Kim et al. [30], and Muralles et al. [31]. Most of these potentials were developed to reproduce the main characteristics of the martensitic transformation close to the equiatomic composition. For the results of MD simulations to be predictive when simulating melting and solidification processes, the employed interatomic potential needs to be able to reproduce the experimental CM phase diagram to obtain the correct solute partitioning and slopes of solidus and liquidus lines. To the best of our knowledge, currently, there is no interatomic potential that accurately reproduces the CM phase diagram in binary Ti-Ni alloys.

In the present study, building on the Ni and Ti potentials developed by Ko et al. [29], we developed new unary potentials with improved capability for predicting high temperature properties of Ni and Ti. In addition to providing better predictions of the targeted properties, melting temperature and latent heat, for pure Ti and Ni; the newly developed potentials also improve the prediction of several thermodynamic and transport properties that affect CM equilibrium and kinetic processes, such as density, cohesive energy, diffusion coefficient, and viscosity. We complement the optimization of the unary potentials with the development of a new MEAM potential for the binary Ni-Ti alloy targeting the CM phase diagram for the Ti rich and Ni rich solutions and liquid phase enthalpy mixing. This new binary potential also improves the prediction ofsolid and liquid phase properties at high temperatures. The transferability of the binary potential was also tested by monitoring the crystal structure and the formation energies of stable intermetallic compounds in the phase diagram of Ti-Ni.

As an application of the developed potential, the anisotropic CM interfacial free energy was calculated using MD simulations with the capillary fluctuation method [14], and using the MD calculated CM interfacial free energy and capillary anisotropy as input parameters, we performed atomistically informed phase field (PF) simulations of dendritic growth during solidification of Ti-2atom% Ni. The comparison of PF simulation results with a geometric model for dendrite primary arm spacing revealed that the atomistically informed PF simulations provides an improved prediction of microstructure development compared to using typical assumed values for the capillary anisotropy. [100-102]

II. OPTIMIZATION OF THE INTERATOMIC POTENTIAL

A. MEAM potential

The modified embedded atom method (MEAM) interatomic potential introduced by Baskes [25] is especially suitable for simulation of multi-component systems. Later, Lee and Baskes [28] modified the MEAM potential to take into account the second-nearest neighbor interactions. Details of the MEAM potential can be found in the previously published papers [28, 32, 33] and are only briefly reviewed here. Within the MEAM approach the total energy, E, for a system of atoms is approximated as

$$E = \sum_i F(\bar{\rho}_i) + \frac{1}{2} \sum_{j \neq i} S_{ij} \varphi_{ij}(r_{ij}) \ . \quad (1)$$

The first term on the right-hand side of equation (1) is the embedding energy, which can be interpreted as the energy cost to insert an atom at site i into the background electron density $\bar{\rho}_i$. The background electron density is computed by combining several partial electron density terms with weighting factors $t^{(h)}$ (h=0-3) corresponding to *s*, *p*, *d*, and *f* orbital symmetry, and for convenience $t^{(0)}$ is taken as unity. Each partial electron density is a function of the atomic configuration of the system and the atomic electron density. The atomic electron densities at a distance r are computed as:

$$\rho^{a(h)}(r) = \rho_0 exp\left[-\beta^{(h)}\left(\frac{r}{r^e} - 1\right)\right] \ , \quad (2)$$

where ρ_0 is the atomic electron density scaling factor; r^e is the nearest-neighbor distance in the equilibrium reference structure; and the decay lengths, $\beta^{(h)}$, are element-dependent adjustable parameters. The embedding energy function has the following form:

$$F(\bar{\rho}_i) = \begin{cases} AE^c \bar{\rho}_i \ln(\bar{\rho}_i) & \bar{\rho}_i \geq 0 \\ AE^c \bar{\rho}_i & \bar{\rho}_i < 0 \end{cases} \quad (3)$$

where A is an adjustable dimensionless parameter of order unity and E^c is the cohesive energy of a reference structure. See the references quoted above for complete details.

The second term on the right-hand side of equation (1) includes the screening function, S_{ij}, and the pair potential interaction function, $\varphi_{ij}(r_{ij})$, between atoms i and j separated by distance r_{ij}. The value of

the pair interaction function is not obtained by using a predetermined functional form, but instead it is evaluated from the known values of total energy and the embedding function of an atom in the equilibrium reference structure. The total energy per atom in the equilibrium reference structure, $E^u(R)$, is obtained as a function of the nearest-neighbor distance, R, and the scaled distance, a^*, and is calculated using the modified zero-temperature universal Rose–Vinet equation of state [34] given by:

$$E^u(R) = -E^c(1 + a^* + \delta\frac{r^e}{R}a^{*3})e^{-a^*}, \quad (4)$$

where δ is an adjustable parameter. The scaled distance is related to the nearest neighbor distance by:

$$a^* = \alpha\left(\frac{R}{r^e} - 1\right), \quad (5)$$

where α is a parameter related to the bulk modulus, cohesive energy, and the equilibrium atomic volume in the reference state. The pair interaction is evaluated from the known values of total energy per atom and the embedding energy as a function of the nearest-neighbor distance.

In practice, the range of interactions is limited by using either a screening function or a cut-off procedure. When screening is used, both the atomic electron densities and the pair potential interactions between atoms i and j are multiplied by a screening function, S_{ij}, which has values in the range between 0 and 1 [35]. The two extreme values of $S_{ij} = 0$ and 1 means the interaction between the atoms i and j is fully-screened and non-screened, respectively. In the original MEAM potential only the first nearest-neighbor interactions were considered by employing strong screening functions; the 2NN-MEAM potential also partially considers 2NN interactions by adjusting the screening parameters (C_{min}, C_{max}) so that the many-body screening becomes less severe. A detailed description of the multi-body screening employed in the 2NN-MEAM formalism is presented in Appendix A.

B. Optimization of potential parameters

We developed improved 2NN-MEAM potentials for Ti, Ni, and Ti-Ni binary systems that reliably predict the crystal-melt (CM) interfacial properties for pure and binary systems and the high temperature portions of the binary system equilibrium phase diagram for both nickel-rich and titanium-rich range of

compositions. The parameters of the newly developed potentials were obtained by adjusting them, through a trial and error process, using the initial values of the corresponding parameters for pure Ti and Ni of the 2NN MEAM potential developed by Ko *et al.* [29].

Table 1 compares the melting temperature and latent heat of fusion calculated by molecular dynamics simulations, based on the coexistence method explained by Asadi et al. [36] using the original Ko *et al.* potentials [29], with the experimental values of Valencia and Quested [37]. Details of melting point calculations are in Supplementary Information. As evident from Table 1, the Ko *et al.* potentials underestimate the melting temperatures of Ti by about 225 K and that of Ni by about 164 K. The melting temperature reported by Ko *et al.* [29] for Ti appears to be for the metastable hcp phase since in our MD simulations we obtained a similar value for that phase. In Table 1, all high temperature properties for Ti were calculated considering the stable bcc phase. In addition, Table 1 shows that there are also differences between the experimental and calculated values of latent heat of fusion for both Ti and Ni and the consequence of these differences are significant because the latent heat of fusion is directly related to the driving force for solidification. As such, our approach was based on the premise that the first step towards obtaining an improved potential capable of reproducing the crystal-melt alloy phase diagram starts with improving the melting properties of the pure components.

Table 1 Calculated melting temperature T_m(K), and latent heat of fusion ΔH_f (kJ/mol) for pure Ti and Ni using the 2NN-MEAM potential by Ko et al. [29], and the corresponding data from experiments [37]. Uncertainties are for 95% confidence intervals.

	Ti		Ni	
Property	Experiment	2NN MEAM (Ko *et al.*)	Experiment	2NN MEAM (Ko *et al.*)
T_m	1942	1651; 1716.0 ± 1.9[a]	1728	1892
ΔH_f	14.17	11.7; 9.07[a]	17.48	20.7

[a] Results obtained from our MD simulations using the same interatomic potential

There are 14 independent parameters describing the single element 2NN MEAM potential. Four of these parameters: E^c, r^e, α, and δ, are related to the pair potential term. The other parameters include the scaling factor parameter A; four decay lengths, $\beta^{(h)}$ (h=0-4); and three weighting factors, $t^{(h)}$ (h=1-3) which are related to the embedding potential term. C_{min} and C_{max} are the parameters controlling the many-body screening. In addition, a reference structure must be chosen. The equilibrium reference structure for a single element can be any structure in which individual atoms occupy the sites of a perfect lattice. We chose fcc for Ni, and bcc for Ti which are the equilibrium phases at the melting points. As a rule of thumb, during the iterative tuning of the potential, the parameters that were being adjusted were chosen such that they had a very limited effect on most of the previously fitted properties such as the equilibrium lattice parameter(s), cohesive energy, and elastic constants. In our study, the guiding criteria was to adjust certain potential parameters such that the resulting potential reproduces the melting point and latent heat close to the corresponding experimental values. Other calculated transport and thermo-physical properties such as: diffusion coefficient, density, volume change on melting, etc., were not included in the iterative fitting process; instead they were used as part of the validation process by evaluating how well these calculated values match those measured in experiments. During the iterative procedure of adjustment of parameters, whenever a compromise was needed, the melting point was given the priority over the latent heat of fusion.

In general, it is not possible to relate the melting point and the enthalpy of fusion to one single parameter in the potential. However, it is known that some parameters have strong effects on certain properties. For example, previous studies have shown that for most materials, small modification of the $t^{(3)}$ parameter has a considerable effect on the melting point [36]. Our study shows that, for Ni, when they are modified together, the parameters $t^{(3)}$ and A have a significant effect on the melting temperature and latent heat. Reducing $t^{(3)}$ reduces the background electron density, which consequently reduces the embedding energy which in turn helps the reduction of the melting point. Reducing the parameter A also reduces the embedding energy. Based on this understanding, for Ti, we modified the parameters $t^{(3)}$, C_{min},

and C_{max}, to adjust the potential to accurately predict its melting temperature. As explained in Appendix A, the value of the parameter C at a second neighbor (defined in the ellipse formula) for a perfect bcc crystal is equal to 2. In the original potential, C_{min} and C_{max} values were 0.25 and 1.58 respectively, so the 2NN interactions were not screened. Increasing both C_{min} and C_{max} to 0.28 and 1.61 has a little effect on screening in the solid phase and does not noticeably affect the solid enthalpy. Table 2 presents the potential parameter sets for Ti and Ni.

Table 2 Optimized 2NN MEAM potential parameter sets for pure Ti and Ni systems. The parameters depicted in bold are those that were modified from the original potential of Ko et al. [29]. The cohesive energy of the reference structure, E^c, is in eV/atom and the equilibrium nearest neighbor distance, r^e, is in Å. The reference structures are bcc for Ti and fcc for Ni.

	E^c	r^e	α	A	$\beta^{(0)}$	$\beta^{(1)}$	$\beta^{(2)}$	$\beta^{(3)}$	$t^{(1)}$	$t^{(2)}$	$t^{(3)}$	C_{min}	C_{max}	δ
Ti	4.75	2.85	4.756	0.24	2.2	3.0	4.0	3.0	-18.0	-32.0	**-14.15**	**0.28**	**1.61**	0
Ni	4.45	2.49	5.0607	**0.763**	2.48	1.94	3.46	2.56	2.84	-1.20	**-2.0**	0.95	1.75	0.05

Extension of 2NN-MEAM potentials of the pure Ti and Ni to the corresponding binary alloy system requires the evaluation of the pair interaction between Ti and Ni atoms. Therefore, 13 additional parameters need to be determined. Four parameters; E^c, r^e, α, and δ; are needed for describing the pair potential. One parameter is the atomic electron density factor ρ_0^{Ni}/ρ_0^{Ti} in the embedding energy function. Finally, eight parameters describe the multi-body screening. First, we need to estimate the potential parameters; E^c, r^e, α, and δ; for the reference structure found in the universal equation of state. The reference structure for the binary system can be any simple compound structure in which each type of atom has only the same type of atoms as its second nearest-neighbors [30]. The binary Ti-Ni system has four stable compounds: NiTi (B19'), NiTi (B2), Ni_3Ti, and $NiTi_2$ [38], and some metastable compounds Ni_3Ti_2 and Ni_4Ti_3 [39]. We chose the reference structure to be the NiTi B2 structure, which is stable at high temperatures. The values of E^c, α, and r^e are chosen based on the corresponding experimental data for enthalpy of formation [40], bulk modulus [41] and the lattice constant [42] of the B2 NiTi compound.

The parameter δ is simply taken to be equal to the average of d for each pure element and the parameter ρ_0^{Ni}/ρ_0^{Ti} is kept at unity. There are four C_{min} and four C_{max} parameters remaining which can be modified. The main goal for the developed binary potential is to accurately reproduce the crystal-melt equilibrium coexistence behavior. As such, the fitting procedure favors the prediction of the characteristics of crystal-melt phase diagram and the enthalpy of mixing in the liquid phase. The enthalpy of formation of the stable compounds, melting point of Ni_3Ti and CM phase diagram for Ni_3Ti on the high Ni concentration side, and liquid densities are used to test the performance of the potential. Table 3 presents the optimized potential parameter set for the binary Ti-Ni system. In addition to the 13 parameters mentioned above, Table 3 also includes the cutoff distance parameter r_c, and the switching function range, Δr.

In MD simulations, the interaction between atoms is only considered if the separation between atoms is within a cut-off radius, r_c. This is accomplished by smooth switching of the potentials, over a distance Δr, to approach zero at r_c. In the potential optimization procedure for the binary system, the original cut-off radius of 5 Å was used.

Table 3 Optimized 2NN-MEAM potential parameter set for the binary Ti-Ni system. The parameters depicted in bold are those that were modified from the original potential of Ko et al. [29]. The units are eV/atom for cohesive energy of the reference structure, E^c, and Å for the equilibrium nearest neighbor distance, r^e; cutoff distance, r_c; and switching function range Δr. The reference structure is B2 NiTi.

E^c	**4.93**	$C_{min}^{Ni\text{-}Ti\text{-}Ni}$	**1.70**
r^e	2.614	$C_{min}^{Ti\text{-}Ni\text{-}Ti}$	**1.60**
α	**4.6338**	$C_{min}^{Ni\text{-}Ni\text{-}Ti}$	**0.15**
ρ_0^{Ni}/ρ_0^{Ti}	1	$C_{min}^{Ti\text{-}Ti\text{-}Ni}$	**0.25**
d	0.025	$C_{max}^{Ni\text{-}Ti\text{-}Ni}$	**2.0**

r_c	5.0	$C_{max}^{Ti\text{-}Ni\text{-}Ti}$	**1.70**
Δr	**0.4**	$C_{max}^{Ni\text{-}Ni\text{-}Ti}$	**2.8**
		$C_{max}^{Ti\text{-}Ti\text{-}Ni}$	**1.9**

To illustrate the role of the appropriate choice for r_c and Δr, the interaction energies of Ti-Ti, Ni-Ti, and Ni-Ni atomic pairs as a function of separation distance between atoms were calculated using the original MEAM potential by Ko et al. [29] and the present MEAM potential. Using $\Delta r = 0.1$ Å, which is the value in the original Ko *et al.* potential, leads to large slopes in the energy near the cutoff distance and correspondingly large forces. In order to reduce the force between atoms, Δr is increased from 0.1 to 0.4 Å.

III. ACCURACY AND TRANSFERABILITY OF THE DEVELOPED 2NN-MEAM POTENTIAL FOR Ti, Ni, AND Ti-Ni

When choosing an interaction potential for a MD simulation one should consider both its accuracy and transferability. For these reasons, the physical properties calculated based on the developed MEAM potential are compared with those obtained from a wide variety of DFT and experimental data. Two sets of physical properties are presented in this section. The first set includes the properties that are considered in the parameter optimization procedure, and therefore they are indicative of the accuracy of the developed potential, and second set of properties were used for the assessment of transferability of the newly developed potential. All MD simulations were performed using the LAMMPS software package [43]. For the sake of clarity, the details pertaining to the simulation methodologies that were used for the calculations of various properties will not be discussed here. Instead, we provide the necessary references, which contain the details of these simulation methodologies. This section is divided up into two main sub-sections; the first sub-section deals with testing the transferability and accuracy of the unary potentials and the second sub-section focuses on the same issues pertaining to the binary potential.

A. Physical properties of pure Ti and Ni

1. Solid phase

Bulk and defect properties at 0 K

The calculated bulk, elastic, and various defect properties for Ti and Ni are shown in Table 4 and Table 5. The corresponding data is compared with the results from DFT, experiments, and those obtained by using the original Ko et al. potential. For both Ti and Ni, in the fitting procedure of the potentials, the experimental cohesive energies were considered more reliable than the DFT values. Both the present and the Ko et al. potentials for Ni yield very similar results. Moreover, it appears that the present potentials for both Ti and Ni underestimate C_{44} by 15% and 33%, respectively. As the main objective of these potentials is to represent the CM interface properties, the mismatch between the shear modulus obtained from simulations and the values obtained from DFT calculations or experimental data was not considered a major issue. The calculated surface energies have maximum discrepancies of 35% for Ti for the $(11\bar{2}0)$ plane and 17.3% for Ni for the (111) plane. Despite these discrepancies, overall, the comparison of the surface energy results, obtained by using the two potential sets, shows improvement when using the presently developed potential.

Table 4 Calculated bulk and defect properties of pure Ti using the present 2NN-MEAM potential, in comparison with experiment data, DFT data, and previous MEAM potential by Ko et al. [29]. The following properties are listed: the cohesive energy E_c (eV/atom); the lattice constant a and c (Å) and the ratio of c/a; the bulk modulus

and elastic constants C_{11}, C_{12}, C_{13}, C_{33}, and C_{44} (GPa); the vacancy formation energy E_f^{vac} (eV); the surface energies (erg/cm^2) for the orientations indicated by the superscripts, and the structural energy differences ΔE (eV/atom).

Property	Experiment	DFT	2NN-MEAM (Ko *et al.* [29])	2NN-MEAM (present)
E_c	4.87 [a]	5.27 [b]	4.86	4.83
a	2.95 [c]	2.93 [b]	2.92	2.92
c	4.68 [c]	4.65 [b]	4.69	4.73
c/a	1.59 [c]	1.59 [b]	1.60	1.62
B	109.7 [d]	113.7 [e]	109.7	110
C_{11}	176.1 [d]	172 [e]	170	158
C_{12}	86.9 [d]	82 [e]	80.4	108
C_{13}	68.3 [d]	75 [e]	74.8	66.7
C_{33}	190.5 [d]	190 [e]	187.1	198
C_{44}	50.8 [d]	45 [e]	42.1	33.9
E_f^{vac}	1.27 [f]	2.045 [b]	1.46	1.83
$E_{surf}^{(0001)}$	1920 [g, k], 2100 [h, k]	1939 [e]	2032	2006
$E_{surf}^{(1\bar{1}00)}$	-	2451 [e]	2307	2255
$E_{surf}^{(11\bar{2}0)}$	-	1875 [e]	2711	2538
$\Delta E_{hcp\rightarrow fcc}$		0.059 [b]	0.011	0.002
$\Delta E_{hcp\rightarrow bcc}$		0.108 [b]	0.078	0.054

[a] Reference [44]. [b] Reference [29]. [c] Reference [45]. [d] Reference [46]. [e] Reference [47].
[f] Reference [48]. [g] Reference [49]. [h] Reference [50]. [k] The experimental value is for polycrystalline solid.

Table 5 Calculated bulk and defect properties of pure Ni using the present 2NN-MEAM potential, in comparison with experimental data, DFT data, and previous MEAM potential by Ko et al. [29] The following properties are listed: the cohesive energy E_c (eV/atom); the lattice constant a (Å); the bulk modulus and elastic constants C_{11},

C_{12}, and C_{44} (GPa); the vacancy formation energy E_f^{vac} (eV); the surface energies (erg/cm^2) for the orientations indicated by the superscripts and the structural energy differences ΔE (eV/atom)

Property	Experiment	DFT	2NN-MEAM (Ko *et al.* [29])	2NN-MEAM (present)
E_c	4.45 [a]	4.842 [b]	4.45	4.45
a	3.520 [c]	3.524 [b]	3.521	3.521
B	187.6 [d]	190.9 [b]	185.9	185.9
C_{11}	261.2 [d]	266.1 [b]	260.4	260.9
C_{12}	150.8 [d]	155.1 [b]	148.6	148.3
C_{44}	131.7 [d]	128.5 [b]	111.1	112
E_f^{vac}	1.6 [e]	1.41 [b]	1.51	1.35
$E_{surf}^{(100)}$	2240 [f, h]	2426 [g]	2085	2108
$E_{surf}^{(110)}$		2368 [g]	2148	2095
$E_{surf}^{(111)}$		2011 [g]	1630	1662
$\Delta E_{fcc\rightarrow bcc}$		0.093 [b]	0.088	0.071
$\Delta E_{fcc\rightarrow hcp}$		0.026 [b]	0.01	0.009

[a] Reference [44]. [b] Reference [29]. [c] Reference [51]. [d] Reference [46]. [e] Reference [52].
[f] Reference [49]. [g] Reference [53]. [h] The experimental value is for a crystalline solid.

Titanium phase stability

The crystal structure of Ti at room temperature is hcp (α) phase [54]. At about 1155 K, Ti undergoes an allotropic phase transformation to a bcc (β) phase, which remains stable up to the melting temperature. In this study the allotropic transition temperature for both the original and the present potential is calculated using the method presented by Sun et al. [55] which is based on the Gibbs-Helmholtz equation shown below:

$$\int_{T^{hcp\rightarrow bcc}}^{T_m^{bcc}} \frac{\Delta H^{hcp\rightarrow bcc}(T)}{T^2}\,dT + \int_{T_m^{bcc}}^{T_m^{hcp}} \frac{\Delta H_m^{hcp}(T)}{T^2}\,dT = 0\,, \tag{6}$$

where, $T^{hcp\rightarrow bcc}$ and $\Delta H^{hcp\rightarrow bcc}$ are the hcp to bcc allotropic phase transition temperature and the temperature dependent enthalpy difference between the phases, T_m^{bcc} and T_m^{hcp} are the melting temperatures of the bcc and hcp phases, and ΔH_m^{hcp} is the temperature dependent enthalpy difference between the hcp crystal and liquid phases.

The allotropic hcp to bcc phase transition temperature and enthalpy of transition are presented in Table 6. The present potential, as well as the original potential by Ko et al. [29], predicts a stable bcc (β)

phase at high temperature. The experimental transition temperature is approximately 1155 K [56] and the corresponding values obtained using the present and original potentials are 1312 and 1481 K respectively; values which deviate by 13% and 28% respectively from experiment data. The enthalpy of transition for both potentials are in good agreement with the experiment data [57-59], but they differ considerably from the DFT result [60] which is 2-3 times higher than experimental values.

Table 6 Allotropic transition temperature, $T^{hcp\rightarrow bcc}$ (K), and enthalpy of transition, $\Delta H_{hcp-bcc}(T^{hcp\rightarrow bcc})$ (kJ/mol), for titanium from experiments, DFT, obtained by using the original 2NN-MEAM potential by Ko et al. [29], and by using the present 2NN-MEAM potential.

Property	Experiment	DFT	2NN-MEAM (Ko *et al. [29]*)	2NN-MEAM (present)
$T_{hcp-bcc}$	1155 [a]	-	1481.7	1312.3
$\Delta H_{hcp-bcc}$	3.2 [b] ; 4.17 [c] ; 4.30 [d]	8.97 [e]	3.18	2.86

[a] Reference [56] [b] Reference [57] [c] Reference [58] [d] Reference [59] [e] Reference [60]

2. Liquid phase

Thermo-physical, and transport properties at the melting point

Table 7 presents the summary of various thermo-physical and transport properties of pure Ti and Ni at the melting point obtained from experiments and calculated from the current potential and the one developed by Ko et al. The crystal-melt (CM) coexistence approach is used for calculation of the melting point. Details of this method are presented in the paper by Asadi et al. [36]. As mentioned before, the optimization of the present unary potentials is performed to primarily obtain a good fit of the melting points and latent heats. However, for Ti we found that it was difficult to match both the melting point and the latent heat simultaneously. Therefore, the latent heat for Ti with our potential is significantly improved but still smaller than the experimental value while we match the experimental melting point. For Ni, we were able to match both the experimental melting temperature and latent heat closely.

The comparison of the volume change upon melting, density, viscosity, diffusivity, and the enthalpy of the liquid phase with the experimental values and the values calculated with the original potential [29]

shows that most properties are improved with exceptions for the Ti diffusivity, Ni density, and Ni enthalpy.

Table 7 Various thermo-physical and transport properties of pure Ti and Ni at their melting points calculated based on the present 2NN-MEAM potential, the potential of Ko et al. [29], and obtained from experiments. The following properties are listed: melting temperature, T_m (K); latent heat of fusion, ΔH_f (kJ/mol); volume change upon melting normalized by the volume of the solid phase, $\Delta V_m/V_s$; density of liquid, ρ_L (g/cm^3); shear viscosity of liquid, η_L (mPa.s); self-diffusivity of liquid, D_L (10^{-5}cm^2/s); and enthalpy of liquid, h_L (kJ/mol). Uncertainties are for 95% confidence intervals.

Property	Ti			Ni		
	Experiment	2NN MEAM (Ko *et al.* [29])	2NN MEAM (present)	Experiment	2NN MEAM (Ko *et al.* [29])	2NN MEAM (present)
T_m	1941 [a]	1716.0 ± 1.9	1942.6 ± 2.6	1728 [a]	1892	1726.7 ± 2.2
ΔH_f	14.15 [b]	9.07	11.45	17.48 [b]	20.7	17.41
$\Delta V_m/V_s(\%)$	2.817 [c]	1.60	1.62	4.5 [d]	7.0	6.1
ρ_L	4.14 [c]	4.25	4.20	7.795 [e]	7.816	7.819
η_L	3.25 [f]	3.024	3.73	4.7 [f]	7.26	6.3
D_L	4.922 [g]	5.73	4.733	3.27 [g]	2.52	2.83
h_L	-399.8 [h]	-405.652	-400.6	-361.6 [h]	-362.9	-364.9

[a] Reference [37] [b] Reference [61] [c] Reference [62] [d] Reference [63]
[e] Reference [64] [f] Reference [65] [g] Reference [66] [h] Reference [67]

Temperature-dependence of density and surface tension

The variation of density and surface tension with temperature for both Ti and Ni in the liquid phase were calculated by MD simulations using both the present and the original potential of Ko et al. The details of the simulation methodologies can be found in the Supplemental Material. Over a limited range of temperatures, both density and surface tension can be assumed to be linear functions of temperature:

$$\rho = \rho_m + d\rho/dT\ (T - T_m)\ , \tag{7}$$

$$\sigma = \sigma_m + d\sigma/dT\ (T - T_m)\ , \tag{8}$$

where ρ_m and σ_m are the density and surface tension at the melting point, and $d\rho/dT$ and $d\sigma/dT$ are the temperature coefficients of density and surface tension, respectively. Table 8 presents the comparison of these parameters obtained from MD simulations using both the present potential and the original potential of Ko *et al*. compared to those obtained from experiments.

The temperature in these calculations was varied from 1833 K to 2103 K for Ti and from 1620 K to 1782 K for Ni. In the case of Ti, the comparison of the MD calculated density coefficients, based on the original and the present MEAM potential, and the experimental data reveals a noticeable improvement when using of the present potential; specifically, densities calculated using the present potential show a maximum deviation of less than 1.7% from experimental data. For Ni, the densities calculated using both the original and present MEAM potential are very close to each other and are in good agreement with the experimental data.

Table 8: Surface tension at the melting point, $\sigma_m(mJm^{-2})$; surface tension temperature coefficient, $d\sigma/dT(mJm^{-2}K^{-1})$; density at the melting point, $\rho_m(gcm^{-3})$; and the density temperature coefficient, $d\rho/dT(g\ cm^{-3}\ K^{-1})$, calculated using the present potential in comparison with the original potential and experimental [68-71] results for Ti and Ni

		Ti			Ni		
Property	Coefficients	Experiment	2NN-MEAM (Ko *et al.*)	2NN-MEAM present	Experiment	2NN-MEAM (Ko *et al.*)	2NN-MEAM present
ρ	ρ_m	4.1426 [a]	4.251	4.2049	7.795[b]	7.816	7.819
	$d\rho/dT$	-0.000217 [a]	-0.000091	-0.000141	-0.00066 [b]	-0.00067	-0.00065
σ	σ_m	1.557 [c]	2.15938	2.02	1.7952 [d]	1.15	1.2
	$d\sigma/dT$	-0.156 [c]	-0.04	-0.09	-0.35 [d]	-0.266	-0.303

[a] Reference [68] [b] Reference [69] [c] Reference [70] [d] Reference [71]

The surface tensions are not accurate for either the original or present potential, but the present potentials improves the agreement with experiment. For Ni, the present potential underestimates the surface tension by approximately 35 %, but it still shows an improvement when compared with the 40% discrepancy obtained when using the original potential. In the case of Ti, the discrepancy between the surface tensions calculated based on the present potential and the experiment is about 33%, but it represents a 12% improvement when compared with the results obtained from MD calculations based on the original potential.

Temperature-dependent transport properties

Two temperature dependent transport properties: diffusivity and viscosity of the liquid phase were calculated by MD simulation using both the present and original potential by Ko et al. The details of the simulation methodologies can be found in the Supplemental Material. In the temperatures ranges considered, both the diffusion coefficient and viscosity are assumed to have an Arrhenius temperature dependence [72] given by:

$$D = D_0 \exp(-\frac{E_D}{k_B T}) \quad , \tag{9}$$

$$\eta = \eta_0 \exp(\frac{E_\eta}{k_B T}) \quad , \tag{10}$$

where, E_D, and E_η are the activation energies for diffusion and viscous flow respectively, and D_0 and η_0 are constants. Table 9 presents the comparison of the parameters entering equations (9) and (10) as obtained from MD simulations using both the present and the original potential of Ko *et al*. and those obtained from experiments [65, 72] .

The comparison of experimental and MD-calculated diffusivity parameters (pre-exponential factor and activation energy) in the liquid phase shows that there is a considerable improvement when using the present MEAM potential compared to using the original potential. Moreover, it should be noted that for Ti the simulation data based on the present potential is very close to data from the ab-initio calculations [73]. For instance, the diffusivity values predicted by ab-initio and our potential at T= 1950 K are 5.0, and 4.82 ($\times 10^{-9}$ m^2/s), respectively. This should be viewed with caution though, since in the case of Ni the ab-initio results [74] for diffusivity parameters are higher than the values reported in simulations using both potentials as well as experimental data. As an example we can point to the diffusivity values of 2.68, and 2.26 ($\times 10^{-9}$ m^2/s) predicted by ab-initio and our potential at T= 1620 K.

Viscosity calculations for Ti when using both the present and original potential are in reasonable agreement with the experimental [65] and ab-initio data [73]. In the case of Ni, the comparison of the MD

simulation results based on both potentials with experimental [65] and ab-initio [74] data shows an improvement in the MD-calculated viscosity using the present potential.

Table 9 The activation energy for diffusion, $E_D(eV/atom)$, constant coefficient $D_0(\times 10^{-8}cm^2/s)$, activation energy for viscosity, $E_\eta(eV/atom)$, constant coefficient $\eta_0(mPa.s)$ calculated using the present and the original potential by Ko et al. [29] and experimental results[65, 72] for Ti and Ni

		Ti			Ni		
Property	Coefficients	Experiment	2NN-MEAM (Ko *et al.*)	2NN-MEAM present	Experiment	2NN-MEAM (Ko *et al.*)	2NN-MEAM present
D	E_D	0.43 [a]	0.338	0.393	0.47 [a]	0.533	0.498
	D_0	6.56 [a]	4.31	4.98	7.78 [a]	9.011	8.02
η	E_η	0.28 [b]	0.1826	0.24	0.79 [b]	0.427	0.445
	η_0	0.61 [b]	1.015	0.90	0.283 [b]	0.416	0.318

[a] Reference [65, 72] [b] Reference [65]

B. Physical properties of Ti-Ni binary system

The Ti-Ni phase diagram contains a few intermetallic solid phases seen in experiments [75-77] and DFT [78-80] calculations. For the equiatomic NiTi composition, there are two important structures, the so-called B2 and B19' crystal structures [38]. The B2 and B19' structures are related to the austenitic and martensitic phases of NiTi, respectively. Other structures, such as B19 and B33 which are experimentally observed under special conditions such in thermal aging or under high-pressure conditions [81], or are predicted by DFT [79], are not considered in this study. The other stable intermetallic compounds are Ni_3Ti and $NiTi_2$ intermetallic compounds which will be investigated as part of the verification of the transferability of the present MEAM potential for the binary system.

In this section, we evaluate the accuracy and transferability of the developed binary potential by comparing a set of calculated material properties with the available experimental and DFT calculated data. The parameters of the potential for Ti-Ni binary system were optimized based on the experimental data for the phase diagram and enthalpy of mixing in the liquid. The potential was not fitted to the high

temperature properties of the solid-solutions, and other liquid phase properties. Instead, these properties are studied to investigate the transferability of the potential.

1. Solid phase

Physical properties of binary compounds at 0 K

For testing the binary Ti-Ni potential, the physical properties of the solid solutions and binary compounds are very important and must be investigated. Table 10 lists various physical properties of NiTi (B2 and B19' structures), Ni_3Ti, and $NiTi_2$ intermetallic compounds as obtained from: MD calculations based on the present and the original potential of Ko et al., experimental investigations, and DFT calculations. These results show that the present potential reproduces very well the lattice constants, monoclinic angles, and the formation energies for most compounds. Moreover, the cohesive energies of the B2 and B19' structures calculated from MD simulation follow the same trend as that predicted by DFT calculations. The B19' structure has a lower energy than the B2 structure, which means that at 0 K the B19' structure is energetically more favorable. The lattice parameter and the formation energy for $NiTi_2$ matches very well with the corresponding experimental and DFT values. One shortcoming of the current potential is that, very much like DFT calculations, it gives a relatively poor estimate of the enthalpy of formation of Ni_3Ti when compared with the values obtained from experiments and the MD calculations based on Ko et al. potential.

Table 10 Physical properties of Ti-Ni binary compounds at various compositions from experiment data, DFT calculations, and from calculations based on the present 2NN-MEAM potential and the previous MEAM potential by Ko et al. [29]. *The following properties are listed: the lattice constants a, b, c (Å); the monoclinic angle β (degree); the enthalpy of formation ΔE_f (eV/atom).*

Composition	Structure (space group)	property	Experiment	DFT	2NN-MEAM (Ko *et al.* [29])	2NN-MEAM (present)
NiTi	B2 (*P* $m\bar{3}m$)	a	3.016 [a]	3.012 [b], 3.009 [c]	2.99	3.015
		b	4.265 [a]	4.26 [b], 4.255 [c]	4.242	4.264
		c	4.265 [a]	4.26 [b], 4.255 [c]	4.242	4.264
		β	90 [a]	90 [b], 90 [c]	90	90
		ΔE_f	-0.351 [d]	-0.355 [b]	-0.3968	-0.2957
	B19' (*$P2_1/m$*)	a	2.909 [a]	2.945 [b], 2.917 [e]	2.878	2.865
		b	4.114 [a]	4.034 [b], 4.047 [e]	4.129	4.187
		c	4.657 [a]	4.769 [b], 4.780 [e]	4.659	4.616
		β	97.9 [a]	101.8 [b], 100.0 [e]	99.4	97.3
		$E-E_{B2}$		-0.0428 [b], -0.0415 [e]	-0.0341	-0.0329
Ni_3Ti	*DO_{24} ($P6_3/mmc$)*	a	5.101 [f]	5.108 [b]	5.1577	5.175
		c	8.307 [f]	8.337 [b]	8.35	8.366
		ΔE_f	-0.36 [g]	-0.487 [b]	-0.35	-0.266
$NiTi_2$	*$E9_3$ ($F d\bar{3}m$)*	a	11.28 [h]	11.28 [b]	11.3	11.329
		ΔE_f	-0.278 [g]	-0.280 [b]	-0.298	-0.270

[a] Reference [42] [b] Reference [29] [c] Reference [79] [d] Reference [40, 82]
[e] Reference [80] [f] Reference [83] [g] Reference [41] [h] Reference [84]

Enthalpy of formation of binary compounds at high temperature

Any potential used in simulation of solidification of binary alloys should also be able to reproduce a reasonable set of properties of both the solid and liquid alloy phases at high temperature. Since there are experimental values for the formation energies of NiTi, Ni_3Ti, and $NiTi_2$ compounds at 1475, 1202, and 1513 K respectively[77], we performed MD calculations of the energies of formation for the three intermetallic compounds at the same temperatures using both the currently developed and the Ko et al. potentials and the results are in Table 11. The comparison of the MD-calculated values using the two potentials with the experimental results clearly shows that the current potential is better suited for high temperature calculations. Specifically, while the calculations based on Ko et al. potential overestimate

the formation energy of NiTi by 20%, the calculated value based on the present potential deviates by less than 3% from the experimental value. Even though the present potential results for Ni_3Ti deviate by 28% from the experimental value, this is still better than the results obtained based on the Ko et al. potential which predicts that the Ni_3Ti compound melts at 1513 K. In addition, the only 4% difference between the MD calculated value, based on the present potential, and the experimental results for $NiTi_2$ is significantly smaller than the 16% discrepancy obtained when using the Ko et al. potential.

1Table 11 The formation energy, ΔE_f (kJ/mol) of binary compounds NiTi (at 1475 K), Ni_3Ti (at 1513 K), and $NiTi_2$ (at 1202 K), from experiments [77] and calculated using the present 2NN MEAM potential and the original MEAM potential by Ko et al. [29].

Composition	Experiment	2NN MEAM (Ko *et al.* [29])	2NN MEAM (present)
NiTi	-34.0	-42.5	-35.0
Ni_3Ti	-42.9	melts	-30.4
$NiTi_2$	-29.3	-34.0	-30.4

2. Liquid phase

Density of liquid binary alloys

The transferability of the binary potential was tested by comparing the density in the liquid phase for a set of five compositions which include $Ni_{25}Ti_{75}$, $Ni_{40}Ti_{60}$, $Ni_{50}Ti_{50}$, $Ni_{60}Ti_{40}$, and $Ni_{75}Ti_{25}$ with corresponding experimental values [85, 86], As illustrated in Figure 1, the density values obtained by using the binary MEAM potential are in very good agreement with the experiments; the largest discrepancy, which is less than 5%, between the simulation and experimental data was obtained for the $Ni_{60}Ti_{40}$.

Enthalpy of mixing

During fitting, we computed liquid binary alloy enthalpies of mixing to ensure reasonable agreement with experiment [81]. The details of the simulation methodologies can be found in the Supplemental Material. In Figure 2, we compare the liquid binary alloy enthalpies of mixing at 1800 K and 1980 K

with experimental data. The enthalpies of mixing calculated based on the present potential are in good agreement with the experimental data. The minimum values of the enthalpy of mixing obtained from both MD simulations and experiments are located approximately at compositions close to 45 atom % Ti. The agreement between the calculated and experimental values is especially good for the Ni-rich compositions. Overall, the maximum discrepancy between the calculated and experimental values for the Ni-rich and Ti-rich systems are less than about 5% and 16%, respectively.

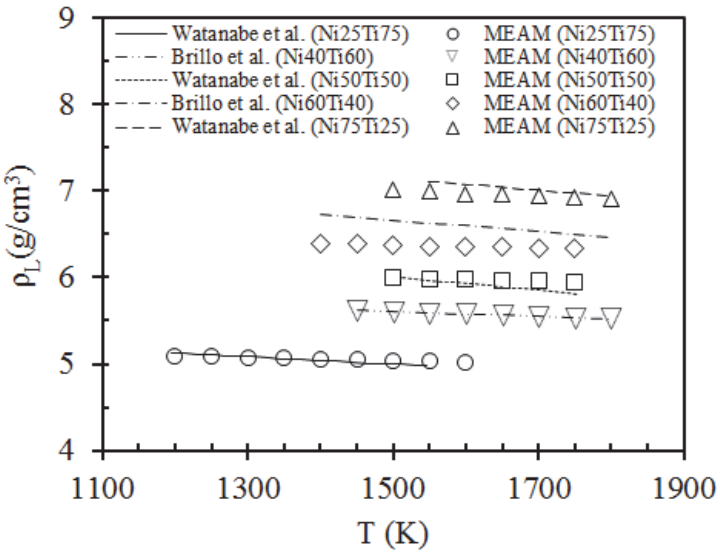

Figure 1 Temperature dependence of the liquid density, ρ_L, for $Ni_{25}Ti_{75}$, $Ni_{40}Ti_{60}$, $Ni_{50}Ti_{50}$, $Ni_{65}Ti_{40}$ and $Ni_{75}Ti_{25}$ compositions calculated using the present 2NN-MEAM potential and from experimental data by Watanabe at al. [85] and Brillo et al. [86].

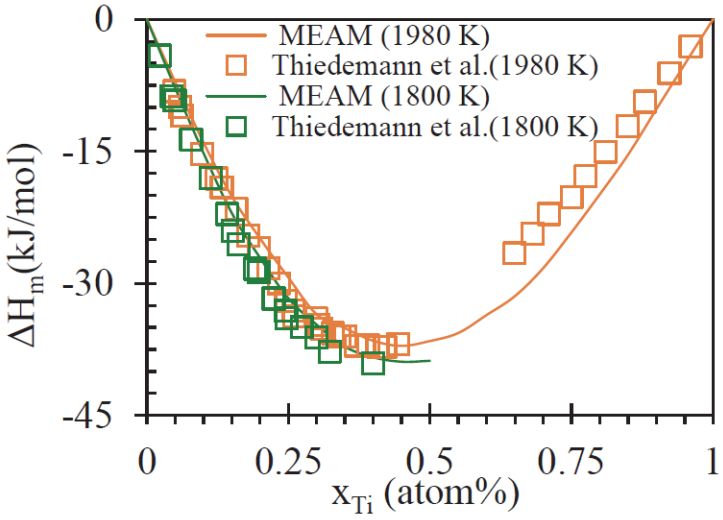

Figure 2 Concentration dependence of the enthalpy of mixing, ΔH_m, in liquid Ni-Ti alloys calculated using the present 2NN-MEAM potential and the experiment data by Thiedemann et al. [87]

3. Crystal-melt phase equilibrium

Phase diagram

As part of the optimization process of the parameters describing the potential, in addition to the enthalpy of mixing, we calculated the CM coexistence portions of the phase diagram for Ti-rich and Ni-rich solid solutions. For reference and comparison with the MD calculations, the entire phase diagram was calculated by using CALPHAD (CALculation of PHAse Diagrams) [88]. Specifically, we utilized the commercial software, Thermo-Calc version 4.1 [89], with the TCBIN binary solutions database under atmospheric pressure. The MD calculated portions of the CM coexistence region of the phase diagram for the Ti-rich portion were determined for concentrations ranging from 0 to 15.7 at% Ni for the liquidus line and from 0 to 7.6 at % Ni for solidus line. For the Ni-rich portion the phase diagram the calculations determined the liquidus line for concentrations ranging from 84.8 to 100 at% Ni, and the solidus line for concentrations ranging from 86.2 to 100 at% Ni. The details of the methodology employed in the MD calculations are given in the Supplemental Material.

Figure 3 shows the comparison of the Ti-rich and Ni-rich CM coexistence portions of the Ti-Ni phase diagram calculated from the MD simulation using the current potential and those obtained from Thermo-

Calc software. As seen from Figure 3, the MD simulations reproduce quite accurately the Ni-rich portion of the phase diagram. For the Ti-rich portion and temperatures in the 1550 K to 1943 K range, the solidus and liquidus curves are approximately straight lines and agree with the Thermo-Calc generated phase diagram but the MD liquidus lines deviates from Thermo-Calc in the 1400 K to 1550 K temperature range. In the higher temperature range of 1550 K to 1943 K, the slopes for the solidus line, m_S, and liquidus line, m_L, derived from the Thermo-Calc calculated phase diagram, were estimated to be equal to 75 K/atom% and 25.7 K/atom%, respectively. The corresponding slopes from the MD calculated phase diagram are m_S = 77.3 K/atom% and m_L = 29.5 K/atom%. For the same temperature range, the partition coefficients from Thermo-Calc and MD-calculated phase diagrams are 0.35 and 0.38 respectively.

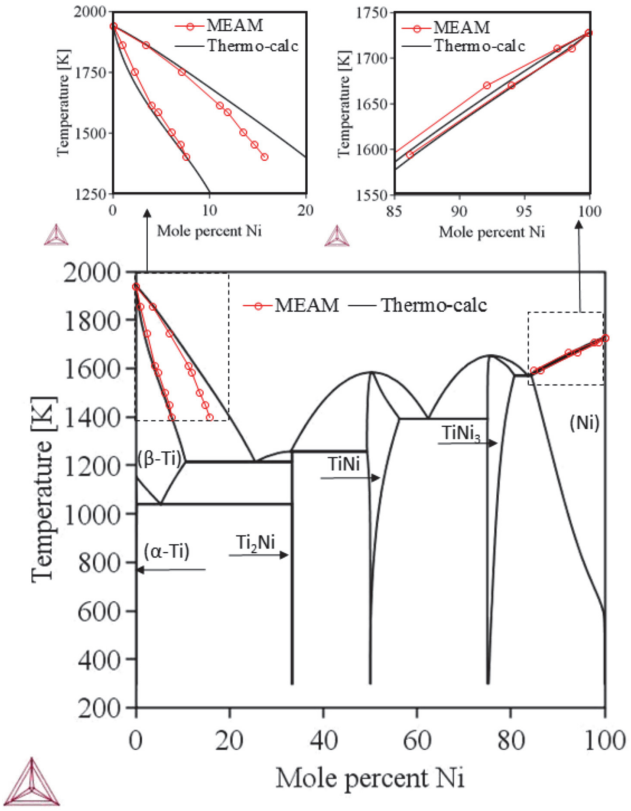

Figure 3 The Ti-rich and Ni-rich portions of Ti-Ni phase diagram calculated using the present MEAM potential compared to the phase diagram based on CALPHAD calculations with the Thermo-Calc software [89].

IV. SIMULATION OF MICROSTRUCTURE EVOLUTION DURING SOLIDIFICATION

In this section, we present an application, that our potential is well suited for, which is the calculation of the anisotropic crystal-melt (CM) interfacial free energy to be used in phase field modeling of alloy solidification. For a crystal with cubic symmetry, the interfacial free energy as a function of CM interface orientation can be represented by the following equation:

$$\gamma = \gamma_0 \left[1 + \delta_1 \left(\sum_{i=1}^{3} n_i^4 - \frac{3}{5}\right) + \delta_2 (3 \sum_{i=1}^{3} n_i^4 + 66 n_1^2 n_2^2 n_3^2 - 17/7)\right] \qquad (11)$$

where γ_0 is the average interfacial free energy, δ_1 and δ_2 are the anisotropy parameters, and n_i are the components of the unit vector, $\hat{n}$, normal to the interface plane [90]. Based on the magnitude and sign of δ_1 and δ_2, either the <100>, <110>, or <111> directions can be the preferred dendrite growth directions. The anisotropy in the CM interfacial properties of a pure material can be perturbed by the addition of alloying elements[91]. Many phase field studies show the importance of the effect of crystalline anisotropy on dendrite shape [92] and growth rate [93]. A major limiting factor of quantitative prediction of microstructure with the phase field simulation approach is the scarcity of available experimental data pertaining to the CM interfacial properties and their anisotropy parameters. The capillary fluctuation [94] is a well-established method for calculating the interfacial free energy. The details of MD simulations and the analysis performed to define the accurate position of interface is explained in detail in our previous work [95]. The only difference in this work compared to [95] is that we used hybrid NPT MD/MC to equilibrate the concentrations in the crystal and melt phases in alloys for 1 ns by using MC to attempt to swap a randomly chosen Ti atom with a randomly chosen Ni atom 500 times after every 5000 MD steps. After this equilibration period, MC swapping was turned off.

Table 12 summarizes the parameters entering equation (11) obtained by a best fit to the MD data of pure Ti and Ti alloyed with 2 and 4 atom% Ni. As a validation of our interfacial free energy simulations, the model of Kaptay (equation 16 in [96]) for pure Ti with the enthalpy of fusion and latent heat obtained using our potential gives an almost identical result for γ_0 of 199 mJ/m^2. The value for pure Ti is near the

upper range of experimental values.[97] The results show that the addition of Ni to the pure alloy decreases the average interfacial free energy, γ_0, but increases the magnitude of both anisotropy parameters, δ_1 and δ_2. For all three studied cases $\delta_1 > 0$ and $\delta_2 < 0$, which means that either the <100> or <110> oriented dendrites will be produced. As δ_1 decreases, the dendrites would prefer to grow in <110> direction rather than <100>. We should note that although the results are over a very limited concentration range, our δ_1 increased with decreasing values of the equilibrium partition coefficient (increasing concentration for our data) while for recently published results for Fe-Cr[15] δ_1 decreased strongly with decreasing equilibrium partition coefficient and is even negative for one concentration. The reason for this difference is not clear but may simply indicate that the behavior of the anisotropy is strongly dependent on the crystal structure of the alloy.

We performed phase field simulations to gain insight into how the interface free energy and the anisotropy parameters affect the dendrite shape and the resulting microstructure during solidification. As the dendrites do not prefer to grow in the <111> direction, we considered that the dendrites will only grow in a plane which we define as the x-y plane and thus performed 2D phase field simulations with a single anisotropy parameter [98]. Fitting the data to single anisotropy parameters gives δ= 0.0047, 0.007 and 0.01 for the pure Ti, and Ti alloys with 2 and 4 atom% Ni, respectively. The anisotropy values are much smaller than the anisotropy values calculated for the FCC metals. Previous MD studies suggest that the crystal structure mostly defines the magnitude of the anisotropy; FCC systems tend to have a larger anisotropy than BCC [13].

Table 12 The average CM interface free energy, γ_0 (mJ/m^2), and anisotropy parameters, δ_1 and δ_2, defined in equation (11) for Ti-X atom% Ni (X = 0, 2, 4). The numbers in the parentheses are the uncertainties of the last significant digits.

	Pure Ti	Ti-2 atom% Ni	Ti-4 atom% Ni
γ_0	198(3)	186(6)	172(3)
δ_1	0.021(5)	0.022(5)	0.024(6)
δ_2	-0.0007(7)	-0.0037(2)	-0.0048(9)

The EFKP phase field model is used in this study is that developed by Echebarria et al.. More details on this model can be found in the reference paper [99]; here only the equations for the phase field, φ, and solute concentration, c, are given:

$$\tau(\theta)\,\frac{\partial\varphi}{\partial t} = \nabla.\left(W(\theta)^2\nabla\varphi\right) - \frac{\partial}{\partial x}\left(W(\theta)W'(\theta)\frac{\partial\varphi}{\partial y}\right) + \frac{\partial}{\partial y}\left(W(\theta)W'(\theta)\frac{\partial\varphi}{\partial x}\right) + \varphi - \varphi^3 - \frac{\lambda}{1-k_e}(1-\varphi^2)^2\left[e^u - 1 - \frac{T-T_0}{m_l c_0/k_e}\right] \quad , \tag{12}$$

$$\frac{\partial c}{\partial t} = \nabla.\left(\left[\frac{1-\varphi}{2}\mathrm{D}_l\right]\{1+k_e-(1-k_e)\varphi\}\frac{c_0}{k_e}\nabla e^u\right) - \frac{W}{2\sqrt{2}}(1-k_e)\frac{c_0}{k_e}\nabla e^u\frac{\partial\varphi}{\partial t}\,\hat{n} \quad . \tag{13}$$

We consider directional solidification where the temperature field is approximated as:

$$T = T_0 + G(y - V_p t)\,, \tag{14}$$

Where, V_p, is the pulling velocity and G is the temperature gradient at the dendrite tip. We can obtain the phase field parameters by using the MD calculated CM interfacial free energy with the thin interface analysis, as explained in the reference [99]. Table 13 summarizes all material properties calculated using MD simulations. These properties are used in the thin interface analysis, considering a coupling constant λ, to obtain the interface attachment time scale, τ, and the interface width, W, for the phase field model.

Table 13 Material properties calculated by MD simulations to use in thin interface analysis for Ti-2 atom% Ni

Equilibrium liquidus slope, m_l (K/atom %)	24
Equilibrium partition coefficient, k_e	0.29
CM interfacial free energy, γ (mJ/m^2)	186
Gibbs-Thomson coefficient, Γ (Km)	2.9×10^{-7}
Liquid diffusion coefficient, D_l ($\times10^{-9}$ m^2/s)	2.76
Equilibrium freezing range, ΔT_0 (K)	34

Figure 4 shows the shapes of the solid phase and the concentration profiles generated during solidification of Ti-2 atom% Ni with a pulling velocity of 0.1 m/s and a temperature gradient of 10^7 K/m and considering three values of the capillary anisotropy parameter. Figure 4 (a) and (b) show the

morphologies and concentration profiles of the simulated systems with the anisotropy parameter calculated from MD simulations. The other two morphologies and concentration profiles correspond to the model systems in which the anisotropies are larger and smaller than the MD-calculated value. Figure 4 (c) and (d) illustrate the effect of using a smaller anisotropy parameter of 0.003 on the dendrite shape and concentration profile. In most phase field simulations, the anisotropy values are assumed to be 0.02 or 0.03 [100-102]. Figure 4 (e) and (f) show the morphology of the dendrites and concentration profile considering an anisotropy parameter of 0.02.

For larger anisotropy, the preferred direction for solidification is <100> which makes the dendrites more elongated in the y-direction, as shown in Figure 4 (e). During the growth competition, the most favorably oriented dendrites with respect to the temperature gradient (y-direction) will survive. If we consider a large value for the capillary anisotropy, more dendrites survive and grow in the y-direction. While for smaller anisotropy, where the dendrites have less preference to grow in y-direction, some dendrites block the growth of the others and this reduces the final number of dendrites that are grown. The curves and branches seen most easily in the high concentration lines in the lower parts of Figure 4 (b), (d), and (f) represent the dendrites which stopped growing or changed their growth direction to that of the adjacent growing dendrites, and those structures are most prevalent when the anisotropy is lowest in Figure 4 (d). In a fixed-size system, we expect to have fewer and thicker dendrites when having a smaller anisotropy while having a larger number of thinner dendrites for larger anisotropy. This will later be studied in detail by analyzing the primary dendritic arm spacing (PDAS).

Figure 4 also suggests that the dendrite growth reaches steady state faster for cases with larger capillary anisotropy. The dendrite shape and concentration profiles in Figure 4 (e) and (f) reached steady state much earlier than the profiles for the other two lower anisotropy values.

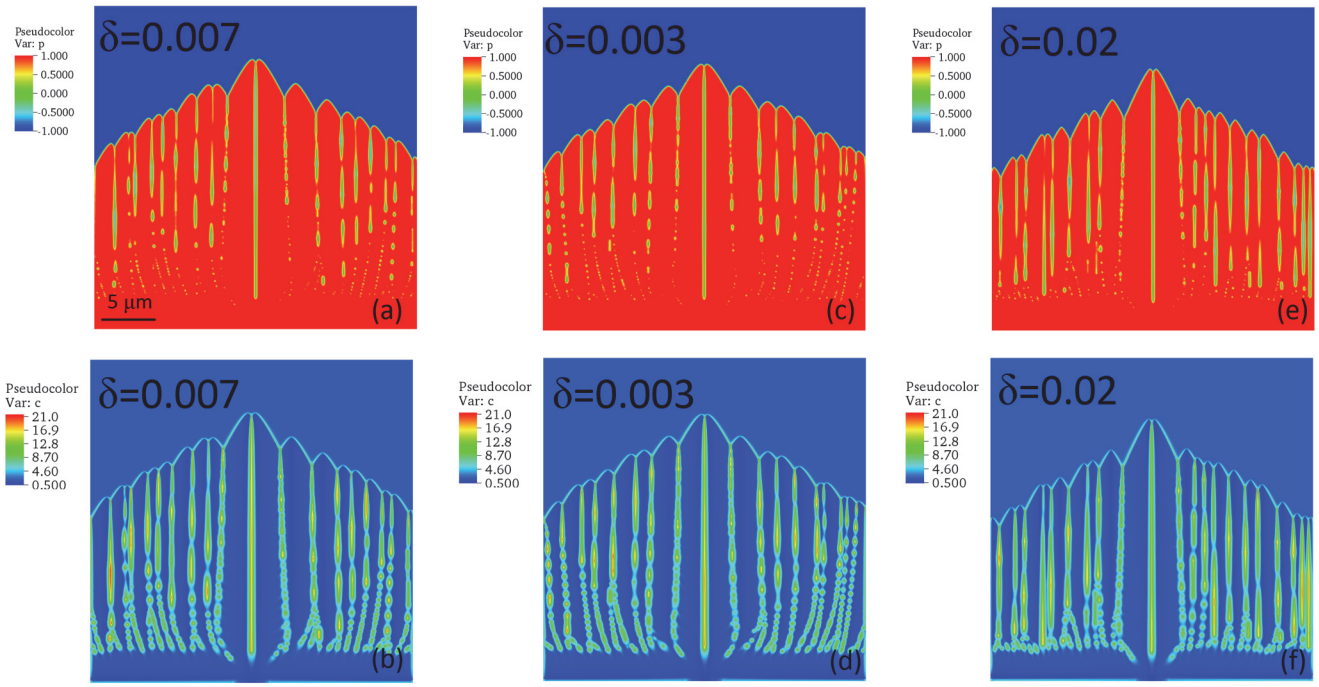

Figure 4 The effect of capillary anisotropy on (top) dendrite morphology and (bottom) concentration profile during solidification of Ti-2 atom% Ni alloy for V_p=0.1 m/s and G=10^7 K/m

The material strength of additively manufactured products depends on the primary dendritic arm spacing and the distribution of the solute between the dendrites. To study the effects of the processing parameters, for the three different anisotropy parameters, multiple simulations are performed where the pulling velocity increases from 0.001 m/s to 0.7 m/s. In all simulations, the temperature gradients have a fixed value of 10^7 K/m. The average PDAS is estimated by dividing the system size by the number of dendrite cells during the steady state growth of dendrites. The simulation results are presented and compared with theoretical models in Figure 5. The two theoretical models used in the comparison are the Hunt-Burden [103] and Kruz-Fisher [1] models which both consider the processing conditions, thermodynamic parameters, and geometry of the cells in their calculations. Burden and Hunt considered only the geometry of the cell tip and obtain the following relation for the arm spacing:

$$PDAS = 2.83(k_e \Gamma \Delta T_0 D_l)^{0.25} G^{-0.5} V^{-0.25} \quad (15)$$

while Kurz and Fisher considered the geometry of the cell tip and trunk and obtained:

$$PDAS = 4.3(\Gamma \Delta T_0 D_l / k_e)^{0.25} G^{-0.5} V^{-0.25} \quad . \tag{16}$$

Comparing the arm spacing calculated by the three simulations shows that using smaller capillary anisotropy in the results in a larger PDAS. As the anisotropy value increases, the spacing between dendrite arms decreases and the arm width becomes smaller, which is in accordance with our visual assessment of Figure 4. The effect of anisotropy on the arm spacing is more obvious as the solidification velocity decreases which results in much coarser dendrites with larger arm spacing. For larger solidification velocities the arm spacing is so small that the effect of anisotropy on the PDAS is not distinguishable

All three simulations have PDAS values which are more consistent with the Kurz-Fisher model than the Hunt-Burden model. The slopes of the linear fits to the data presented in Figure 5 define how the PDAS changes with $V^{-0.25}$ $G^{-0.5}$. Based on both analytical models, the slope only depends on the thermodynamic parameters and for Ti-2 atom% Ni this value is 0.0023 ($m^{0.75}$ $s^{-0.25}$ $K^{0.5}$) in the Kurz-Fisher model. The slopes of the lines, with zero intercept, fitted to the simulation data are 0.0019, 0.0021, and 0.0025 ($m^{0.75}$ $s^{-0.25}$ $K^{0.5}$) for capillary anisotropy equal to 0.02, 0.007, and 0.003, respectively. These results suggest that the MD-calculated anisotropy produces a reasonable slope compared the Kurz-Fisher model and illustrates that if you have a reasonably accurate interatomic potential, calculating the anisotropy using MD instead of simply assuming a value of the anisotropy of 0.02 or 0.03 may lead to improved phase field results.

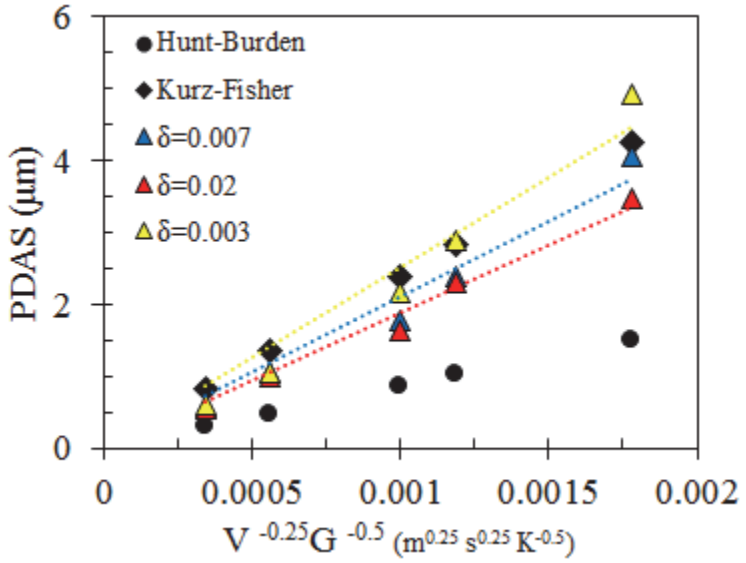

Figure 5 Comparison of simulated PDAS results with the theoretical models of Hunt-Burden [103]and Kurz-Fisher [1] to phase field results with the MD-calculated anisotropy (δ=0.007) and two other anisotropy values (δ=0.003 and δ=0.02). The dotted lines are linear fits where the color of the line is the same as the symbols for the data it was fit to.

V. CONCLUSION

We developed 2NN MEAM potentials for Ti, Ni, and the Ti-Ni binary systems that improve the crystal-melt (CM) interfacial properties for pure and binary systems and the high temperature portions of the binary system CM equilibrium phase diagram for both the nickel-rich and titanium-rich compositions. The new parameters for pure Ti and Ni were obtained by adjusting of the parameters of the 2NN-MEAM potentials developed by Ko *et al.* [29] to fit the melting points and latent heats of fusion. The reliability of the potentials for pure Ti and pure Ni were tested by comparison of various physical quantities including structural properties, elastic constants, point-defect properties, surface energies, temperatures and enthalpies of phase transformations, and thermodynamic and dynamic properties of the liquid phases with experimental and DFT data. Most of the 0 K properties are not affected much by the potential modifications, while most of high temperature properties are improved relative to the original potentials. The binary potential was fit to the liquid enthalpies of mixing and the CM portions of the phase diagram in the Ni-rich and Ti-rich regions. The fitted binary potential for Ti-Ni was also tested

against various non-fitted properties such as lattice parameters, formation energies of different intermetallic compounds, and the temperature dependence of liquid density at various concentrations. As with pure Ni and Ti, most of the high temperature properties of the binary are improved relative to the original potential. The binary Ti-Ni potential accurately captures the CM portions of the equilibrium phase diagram on the Ti-rich side from pure Ti down to about 1550 K and on the Ni-rich side and from pure Ni down to about the eutectic temperature of 1577 K.

The developed potential was applied by calculating the anisotropic CM interfacial free energy as a function of composition, then using the MD-calculated average interfacial free energy and capillary anisotropy as inputs to perform phase field simulations of the Ti-2atom%Ni. The comparison of phase field results with the geometric models reveals the atomistically informed phase field simulations provides a better prediction of microstructure compared to other studied model systems. The BCC alloys have a smaller anisotropy parameters, comparing to FCC alloys, and in phase field simulations the crystal structure of the studied alloy must be considered when choosing the capillary anisotropy parameter. It is shown that using a higher anisotropy value, equal to average value considered in many phase-field studies, underestimates the primary dendritic arm spacing.

ACKNOWLEDGEMENTS

The authors gratefully acknowledge the support from the U.S. National Science Foundation (CIMM Project OIA-1541079). The computer resources were provided by LONI and High Performance Computing at LSU. M.A.Z. would like to acknowledge the funding support from the U.S. National Science Foundation (NSF-CMMI 1537170 and NSF-CMMI 1855491).

VI. Appendix A. Multi-body screening function

In the original MEAM potential, the second-nearest neighbor interactions are neglected. The 2NN-MEAM potential formulations accounts for the second nearest neighbor interactions by using screening functions [33]. Specifically, in this framework a screening factor that defines the range of interaction between atoms i and j, S_{ij}, can take values between 0 and 1; the value of 0 represents full-screening and the value of 1 represents no-screening. The values of S_{ij} depend on the distribution of all atoms, k, which are common neighbors of atoms i, and j. As such, S_{ij} values are the result of individual contributions from all ikj combination that are described by S_{ikj} which in turn are defined by using a simple geometric construction[35]. Consider the atoms i, j, and k all located in the same plane, as shown in Figure A.1 and the origin is set midway between i and j. One can consider an ellipse passing through atoms i, j, and k with the minor axis on the line connecting atoms i and j. Thus, using the length of the minor axis as r_{ij} equal to the distance between atom i, j the equation of this ellipse is given by:

$$x^2 + \frac{y^2}{C} = \left(\frac{1}{2} r_{ij}\right)^2 \quad , \tag{A.1}$$

where parameter C controls the elongation of the ellipse in the y-direction and is given by:

$$C = \frac{2(X_{ik}+X_{kj}) - (X_{ik}-X_{kj})^2 - 1}{1-(X_{ik}-X_{kj})^2} \tag{A.2}$$

where $X_{ik} \equiv \left(r_{ik}/r_{ij}\right)^2$ and $X_{kj} \equiv \left(r_{kj}/r_{ij}\right)^2$. The corresponding values of C for perfect FCC and BCC crystal structures are 1 and 2, respectively. The blue and red lines in Figure A.1 are the ellipses for C values corresponding to perfect BCC and FCC crystal structures.

In 2NN-MEAM potential, the contributing terms, S_{ikj}, are determined by two parameters C_{min} and C_{max}. When the ellipse passing through atoms *i, j*, and *k* is located outside the ellipse defined by C_{max}, it means that the atom *k* does not screen the interaction between atoms *i* and *j* and S_{ikj} will be equal to 1. If the ellipse passing through atoms *i, j*, and *k* is located inside the region delimited by the ellipse defined by C_{min}, it means that the atom *k* fully screens the interaction between atoms *i* and *j* and, S_{ikj} will be equal

to 0. When the ellipse passing through atoms *i, j*, and, *k* is located between the two ellipses defined by C_{max} and C_{min}, S_{ikj} will vary smoothly between 0 and 1. The overall form of S_{ikj} can be written, using the cut-off function of $f_c(x)$, as:

$$S_{ikj} = f_c\left(\frac{C-C_{min}}{C_{max}-C_{min}}\right) \tag{A.3}$$

$$f_c(x) = \begin{cases} 1 & x \geq 1, \\ (1-(1-x)^4)^2 & 0 < x < 1, \\ 0 & x \leq 1, \end{cases} . \tag{A.4}$$

The same radial cut-off function is applied to the pair potential in the form of $f_c((r_c - r)/\Delta r)$, where r_c is the cut-off distance and Δr controls the distance over which the radial cut-off is smoothened from 0 to 1 near r_c. S_{ij} is calculated using equation (A.5) and (A.6).

$$\bar{S}_{ij} = \prod_{k \neq i,j} S_{ikj} \tag{A.5}$$

$$S_{ij} = \bar{S}_{ij} f_c\left(\frac{r_c - r}{\Delta r}\right) \tag{A.6}$$

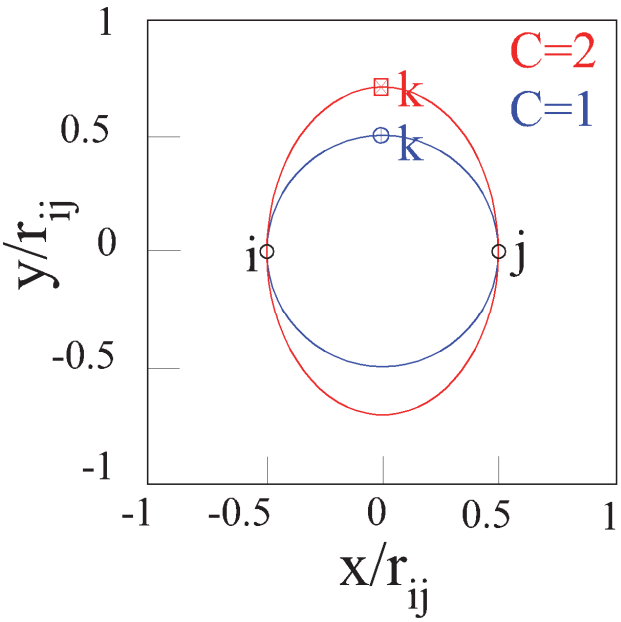

Figure A.1 Graphical depiction of the ellipses used in the definition of contributing term of the screening factor of atoms i ,j by the neighboring atom k for fcc and bcc structures.

REFERENCES

[1] W. Kurz, D.J. Fisher, Dendrite growth at the limit of stability: tip radius and spacing, Acta Metallurgica, 29 (1981) 11-20.
[2] Y.-J. Liang, A. Li, X. Cheng, X.-T. Pang, H.-M. Wang, Prediction of primary dendritic arm spacing during laser rapid directional solidification of single-crystal nickel-base superalloys, Journal of Alloys and Compounds, 688 (2016) 133-142.
[3] X.W. Hu, S.M. Li, W.J. Chen, S.F. Gao, L. Liu, H.Z. Fu, Primary dendrite arm spacing during unidirectional solidification of Pb–Bi peritectic alloys, Journal of Alloys and Compounds, 484 (2009) 631-636.
[4] M. Gäumann, C. Bezençon, P. Canalis, W. Kurz, Single-crystal laser deposition of superalloys: processing–microstructure maps, Acta Materialia, 49 (2001) 1051-1062.
[5] P. Geslin, A. Karma, Numerical investigation of the columnar-to-equiaxed transition using a 2D needle network model.
[6] H.B. Dong, X.L. Yang, P.D. Lee, W. Wang, Simulation of equiaxed growth ahead of an advancing columnar front in directionally solidified Ni-based superalloys, Journal of Materials Science, 39 (2004) 7207-7212.
[7] M.I. Mendelev, M. Asta, M.J. Rahman, J.J. Hoyt, Development of interatomic potentials appropriate for simulation of solid–liquid interface properties in Al–Mg alloys, Philosophical Magazine, 89 (2009) 3269-3285.
[8] J. Monk, Y. Yang, M.I. Mendelev, M. Asta, J.J. Hoyt, D.Y. Sun, Determination of the crystal-melt interface kinetic coefficient from molecular dynamics simulations, Modelling and Simulation in Materials Science and Engineering, 18 (2010) 015004.
[9] Y. Yang, H. Humadi, D. Buta, B.B. Laird, D. Sun, J.J. Hoyt, M. Asta, Atomistic Simulations of Nonequilibrium Crystal-Growth Kinetics from Alloy Melts, Physical Review Letters, 107 (2011) 025505.
[10] J. Hoyt, M. Asta, A. Karma, Method for computing the anisotropy of the solid-liquid interfacial free energy, Physical review letters, 86 (2001) 5530.
[11] T. Frolov, Y. Mishin, Solid-liquid interface free energy in binary systems: Theory and atomistic calculations for the (110) Cu–Ag interface, The Journal of Chemical Physics, 131 (2009) 054702.
[12] M. Asta, C. Beckermann, A. Karma, W. Kurz, R. Napolitano, M. Plapp, G. Purdy, M. Rappaz, R. Trivedi, Solidification microstructures and solid-state parallels: Recent developments, future directions, Acta Materialia, 57 (2009) 941-971.
[13] K.-A. Wu, A. Karma, Phase-field crystal modeling of equilibrium bcc-liquid interfaces, Physical Review B, 76 (2007) 184107.
[14] M. Asta, J.J. Hoyt, A. Karma, Calculation of alloy solid-liquid interfacial free energies from atomic-scale simulations, Physical Review B, 66 (2002) 100101.
[15] K. Ueno, Y. Shibuta, Composition dependence of solid-liquid interfacial energy of Fe-Cr binary alloy from molecular dynamics simulations, Computational Materials Science, 167 (2019) 1-7.
[16] M.W. Finnis, J.E. Sinclair, A simple empirical N-body potential for transition metals, Philosophical Magazine A, 50 (1984) 45-55.
[17] W.S. Lai, B.X. Liu, Lattice stability of some Ni-Ti alloy phases versus their chemical composition and disordering, Journal of Physics: Condensed Matter, 12 (2000) L53.
[18] G. Ren, H. Sehitoglu, Interatomic potential for the NiTi alloy and its application, Computational Materials Science, 123 (2016) 19-25.
[19] D. Mutter, P. Nielaba, Simulation of structural phase transitions in NiTi, Physical Review B, 82 (2010) 224201.
[20] Y. Zhong, K. Gall, T. Zhu, Atomistic study of nanotwins in NiTi shape memory alloys, Journal of Applied Physics, 110 (2011) 033532.

[21] C. Kexel, A.V. Verkhovtsev, G.B. Sushko, A.V. Korol, S. Schramm, A.V. Solov'yov, Toward the Exploration of the NiTi Phase Diagram with a Classical Force Field, The Journal of Physical Chemistry C, 120 (2016) 25043-25052.
[22] M.S. Daw, M.I. Baskes, Embedded-atom method: Derivation and application to impurities, surfaces, and other defects in metals, Physical Review B, 29 (1984) 6443-6453.
[23] D. Farkas, D. Roqueta, A. Vilette, K. Ternes, Atomistic simulations in ternary Ni - Ti - Al alloys, Modelling and Simulation in Materials Science and Engineering, 4 (1996) 359.
[24] Y. Li, J. Li, J. Liu, B. Liu, Atomic approach to the optimized compositions of Ni–Nb–Ti glassy alloys with large glass-forming ability, RSC Advances, 5 (2015) 3054-3062.
[25] M.I. Baskes, Modified embedded-atom potentials for cubic materials and impurities, Physical Review B, 46 (1992) 2727-2742.
[26] H. Ishida, Y. Hiwatari, MD simulation of martensitic transformations in TiNi alloys with MEAM, Molecular Simulation, 33 (2007) 459-461.
[27] K.-I. Saitoh, K. Kubota, T. Sato, Atomic-level structural change in Ni-Ti alloys under martensite and amorphous transformations, 2010.
[28] B.-J. Lee, M.I. Baskes, Second nearest-neighbor modified embedded-atom-method potential, Physical Review B, 62 (2000) 8564-8567.
[29] W.-S. Ko, B. Grabowski, J. Neugebauer, Development and application of a Ni-Ti interatomic potential with high predictive accuracy of the martensitic phase transition, Physical Review B, 92 (2015) 134107.
[30] Y.-K. Kim, H.-K. Kim, W.-S. Jung, B.-J. Lee, Development and application of Ni-Ti and Ni-Al-Ti 2NN-MEAM interatomic potentials for Ni-base superalloys, Computational Materials Science, 139 (2017) 225-233.
[31] M. Muralles, S.-D. Park, S.Y. Kim, B. Lee, Phase transformations, detwinning and superelasticity of shape-memory NiTi from MEAM with practical capability, Computational Materials Science, 130 (2017) 138-143.
[32] B.-J. Lee, J.-H. Shim, M.I. Baskes, Semiempirical atomic potentials for the fcc metals Cu, Ag, Au, Ni, Pd, Pt, Al, and Pb based on first and second nearest-neighbor modified embedded atom method, Physical Review B, 68 (2003) 144112.
[33] B.-J. Lee, M.I. Baskes, H. Kim, Y. Koo Cho, Second nearest-neighbor modified embedded atom method potentials for bcc transition metals, Physical Review B, 64 (2001) 184102.
[34] P. Vinet, J.R. Smith, J. Ferrante, J.H. Rose, Temperature effects on the universal equation of state of solids, Physical Review B, 35 (1987) 1945-1953.
[35] M.I. Baskes, J.E. Angelo, C.L. Bisson, Atomistic calculations of composite interfaces, Modelling and Simulation in Materials Science and Engineering, 2 (1994) 505.
[36] E. Asadi, M. Asle Zaeem, S. Nouranian, M.I. Baskes, Quantitative modeling of the equilibration of two-phase solid-liquid Fe by atomistic simulations on diffusive time scales, Physical Review B, 91 (2015) 024105.
[37] J.J. Valencia, P. Quested, Thermophysical properties, Modeling for Casting and Solidification Processing, 189 (2001).
[38] H. Okamoto, Phase diagrams for binary alloys, ASM International, 268 (2000).
[39] T. Hara, T. Ohba, K. Otsuka, M. Nishida, Phase Transformation and Crystal Structures of Ti₂Ni₃ Precipitates in Ti–Ni Alloys, Materials Transactions, JIM, 38 (1997) 277-284.
[40] O. Kubaschewski, H. Villa, W. Dench, The reaction of titanium tetrachloride with hydrogen in contact with various refractories, Transactions of the Faraday Society, 52 (1956) 214-222.
[41] O. Mercier, K.N. Melton, G. Gremaud, J. Hägi, Single‐crystal elastic constants of the equiatomic NiTi alloy near the martensitic transformation, Journal of Applied Physics, 51 (1980) 1833-1834.

[42] S.D. Prokoshkin, A.V. Korotitskiy, V. Brailovski, S. Turenne, I.Y. Khmelevskaya, I.B. Trubitsyna, On the lattice parameters of phases in binary Ti–Ni shape memory alloys, Acta Materialia, 52 (2004) 4479-4492.
[43] S. Plimpton, Fast Parallel Algorithms for Short-Range Molecular Dynamics, Journal of Computational Physics, 117 (1995) 1-19.
[44] C. Kittel, Introduction to Solid State Physics, 8 ed., Wiley2004.
[45] C.S. Barrett, T.B. Massalski, Structure of metals; crystallographic methods, principles, and data, McGraw-Hill, New York, 1966.
[46] G. Simmons, H. Wang, Single crystal elastic constants and calculated aggregate properties: a handbook, M.I.T. Press, Cambridge, Mass., 1971.
[47] R.G. Hennig, T.J. Lenosky, D.R. Trinkle, S.P. Rudin, J.W. Wilkins, Classical potential describes martensitic phase transformations between the $\ensuremath{\alpha}$, $\ensuremath{\beta}$, and $\ensuremath{\omega}$ titanium phases, Physical Review B, 78 (2008) 054121.
[48] E. Hashimoto, E.A. Smirnov, T. Kino, Temperature dependence of the Doppler-broadened lineshape of positron annihilation in α-Ti, Journal of Physics F: Metal Physics, 14 (1984) L215.
[49] W.R. Tyson, W.A. Miller, Surface free energies of solid metals: Estimation from liquid surface tension measurements, Surface Science, 62 (1977) 267-276.
[50] F.R.d. Boer, R. Boom, W.C.M. Mattens, A.R. Miedema, A.K. Niessen, Cohesion in metals : transition metal alloys, North-Holland, Amsterdam, 1989.
[51] R.J. Birgeneau, J. Cordes, G. Dolling, A.D.B. Woods, Normal Modes of Vibration in Nickel, Physical Review, 136 (1964) A1359-A1365.
[52] W. Wycisk, M. Feller-Kniepmeier, Quenching experiments in high purity Ni, Journal of Nuclear Materials, 69-70 (1978) 616-619.
[53] L. Vitos, A.V. Ruban, H.L. Skriver, J. Kollár, The surface energy of metals, Surface Science, 411 (1998) 186-202.
[54] R. Namakian, G. Voyiadjis, An atomic displacive model for {1012}〈1011〉 twinning in hexagonal close packed metals with the emphasis on the role of partial stacking faults in formation of {1012} twins, Acta Materialia, 150 (2018).
[55] D.Y. Sun, M.I. Mendelev, C.A. Becker, K. Kudin, T. Haxhimali, M. Asta, J.J. Hoyt, A. Karma, D.J. Srolovitz, Crystal-melt interfacial free energies in hcp metals: A molecular dynamics study of Mg, Physical Review B, 73 (2006) 024116.
[56] A. Cezairliyan, A. Miiller, Thermodynamic Study of the a~{3 Phase Transformation in Titanium by Pulse Heating Method, JOURNAL OF RESEARCH of the National Bureau of Standards, 83 (1978).
[57] M. Cormier, F. Claisse, Beta-alpha phase transformation in Ti and Ti · O alloys, Journal of the Less Common Metals, 34 (1974) 181-189.
[58] P.D. Desai, Thermodynamic properties of titanium, International Journal of Thermophysics, 8 (1987) 781-794.
[59] M. Martynyuk, V. Tsapkov, Electric resistance, enthalpy and phase transformations of titanium, zirconium and hafnium during pulse heating, Izvestiya Akademii Nauk SSSR, Metally, DOI (1974) 181-188.
[60] S.R. Nishitani, H. Kawabe, M. Aoki, First-principles calculations on bcc–hcp transition of titanium, Materials Science and Engineering: A, 312 (2001) 77-83.
[61] J.A. Dean, N.A. Lange, Lange's handbook of chemistry, McGraw-Hill, New York :, 1973.
[62] E.Y. Kulyamina, V.Y. Zitserman, L.R. Fokin, Titanium Melting Curve: Data Consistency Assessment, Problems and Achievements, Technical Physics, 63 (2018) 369-373.
[63] E.A. Brandes, G.B. Brook, 14 - General physical properties, Smithells Metals Reference Book (Seventh Edition), Butterworth-Heinemann, Oxford, 1992, pp. 14-11-14-43.

[64] J. Brillo, I. Egry, Density Determination of Liquid Copper, Nickel, and Their Alloys, International Journal of Thermophysics, 24 (2003) 1155-1170.
[65] T. Ishikawa, P.-F. Paradis, J.T. Okada, Y. Watanabe, Viscosity measurements of molten refractory metals using an electrostatic levitator, Measurement Science and Technology, 23 (2012) 025305.
[66] J. Horbach, R.E. Rozas, T. Unruh, A. Meyer, Improvement of computer simulation models for metallic melts via quasielastic neutron scattering: A case study of liquid titanium, Physical Review B, 80 (2009) 212203.
[67] C.B. Alcock, V.P. Itkin, M.K. Horrigan, Vapour Pressure Equations for the Metallic Elements: 298–2500K, Canadian Metallurgical Quarterly, 23 (1984) 309-313.
[68] H. Wang, S. Yang, B. Wei, Density and structure of undercooled liquid titanium, Chinese Science Bulletin, 57 (2012) 719-723.
[69] Y. Hanbyeol, P. Cheolmin, J. Sangho, L. Sooheyong, L. Geun Woo, Uncertainty evaluation for density measurements of molten Ni, Zr, Nb and Hf by using a containerless method, Metrologia, 52 (2015) 677.
[70] P.-F. Paradis, T. Ishikawa, S. Yoda, Non-Contact Measurements of Surface Tension and Viscosity of Niobium, Zirconium, and Titanium Using an Electrostatic Levitation Furnace, International Journal of Thermophysics, 23 (2002) 825-842.
[71] S. Sauerland, G. Lohöfer, I. Egry, Surface tension measurements on levitated liquid metal drops, Journal of Non-Crystalline Solids, 156-158 (1993) 833-836.
[72] A. Meyer, The measurement of self-diffusion coefficients in liquid metals with quasielastic neutron scattering, EPJ Web of Conferences, 83 (2015) 01002.
[73] B.G. del Rio, O. Rodriguez, L.E. González, D.J. González, First principles determination of static, dynamic and electronic properties of liquid Ti near melting, Computational Materials Science, 139 (2017) 243-251.
[74] H. Zhang, S.L. Shang, W.Y. Wang, Y. Wang, X.D. Hui, L.Q. Chen, Z.K. Liu, Structure and energetics of Ni from ab initio molecular dynamics calculations, Computational Materials Science, 89 (2014) 242-246.
[75] J. Frenzel, A. Wieczorek, I. Opahle, B. Maaß, R. Drautz, G. Eggeler, On the effect of alloy composition on martensite start temperatures and latent heats in Ni–Ti-based shape memory alloys, Acta Materialia, 90 (2015) 213-231.
[76] Y. Esin, M. Valishev, A. Ermakov, P. Gel'd, M. Petrushevskii, The Enthalpies of Formation of Liquid Germanium--Titanium and Nickel--Titanium Alloys, Russ. J. Phys. Chem., 55 (1981) 421-422.
[77] J.C. Gachon, J. Hertz, Enthalpies of formation of binary phases in the systems FeTi, FeZr, CoTi, CoZr, NiTi, and NiZr, by direct reaction calorimetry, Calphad, 7 (1983) 1-12.
[78] A. Pasturel, C. Colinet, D.N. Manh, A.T. Paxton, M. van Schilfgaarde, Electronic structure and phase stability study in the Ni-Ti system, Physical Review B, 52 (1995) 15176-15190.
[79] X. Huang, G.J. Ackland, K.M. Rabe, Crystal structures and shape-memory behaviour of NiTi, Nature Materials, 2 (2003) 307.
[80] D. Holec, M. Friák, A. Dlouhý, J. Neugebauer, Ab initio study of pressure stabilized NiTi allotropes: Pressure-induced transformations and hysteresis loops, Physical Review B, 84 (2011) 224119.
[81] M. Kök, F. Dağdelen, A. Aydoğdu, Y. Aydoğdu, The change of transformation temperature on NiTi shape memory alloy by pressure and thermal ageing, Journal of Physics: Conference Series, IOP Publishing, 2016, pp. 012011.
[82] J.C. Gachon, M. Notin, J. Hertz, The enthalphy of mixing of the intermediate phases in the systems FeTi, CoTi, and NiTi by direct reaction calorimetry, Thermochimica Acta, 48 (1981) 155-164.
[83] A. Taylor, R.W. Floyd, Precision measurements of lattice parameters of non-cubic crystals, Acta Crystallographica, 3 (1950) 285-289.

[84] G.A. Yurko, J.W. Barton, J.G. Parr, The crystal structure of Ti2Ni, Acta Crystallographica, 12 (1959) 909-911.
[85] M. Watanabe, M. Adachi, H. Fukuyama, Density measurement of Ti-X(X=Cu, Ni) melts and thermodynamic correlations, 2018.
[86] J. Brillo, T. Schumacher, K. Kajikawa, Density of Liquid Ni-Ti and a New Optical Method for its Determination, Metallurgical and Materials Transactions A, 50 (2019) 924-935.
[87] U. Thiedemann, M. Rösner-Kuhn, K. Drewes, G. Kuppermann, M.G. Frohberg, Temperature dependence of the mixing enthalpy of liquid Ti–Ni and Fe–Ti–Ni alloys, Journal of Non-Crystalline Solids, 250-252 (1999) 329-335.
[88] L. Kaufman, J. Ågren, CALPHAD, first and second generation – Birth of the materials genome, Scripta Materialia, 70 (2014) 3-6.
[89] J.-O. Andersson, T. Helander, L. Höglund, P. Shi, B. Sundman, Thermo-Calc & DICTRA, computational tools for materials science, Calphad, 26 (2002) 273-312.
[90] J.J. Hoyt, M. Asta, Atomistic computation of liquid diffusivity, solid-liquid interfacial free energy, and kinetic coefficient in Au and Ag, Physical Review B, 65 (2002) 214106.
[91] J. Friedli, J.L. Fife, P. Di Napoli, M. Rappaz, Dendritic Growth Morphologies in Al-Zn Alloys—Part I: X-ray Tomographic Microscopy, Metallurgical and Materials Transactions A, 44 (2013) 5522-5531.
[92] W.J. Boettinger, S.R. Coriell, A.L. Greer, A. Karma, W. Kurz, M. Rappaz, R. Trivedi, Solidification microstructures: recent developments, future directions, Acta Materialia, 48 (2000) 43-70.
[93] A. Karma, W.J. Rappel, Numerical Simulation of Three-Dimensional Dendritic Growth, Phys Rev Lett, 77 (1996) 4050-4053.
[94] J.J. Hoyt, M. Asta, A. Karma, Method for Computing the Anisotropy of the Solid-Liquid Interfacial Free Energy, Physical Review Letters, 86 (2001) 5530-5533.
[95] S. Kavousi, B.R. Novak, M.A. Zaeem, D. Moldovan, Combined molecular dynamics and phase field simulation investigations of crystal-melt interfacial properties and dendritic solidification of highly undercooled titanium, Computational Materials Science, 163 (2019) 218-229.
[96] G. Kaptay, On the solid/liquid interfacial energies of metals and alloys, Journal of Materials Science, 53 (2018) 3767-3784.
[97] G.W. Lee, S. Jeon, C. Park, D.-H. Kang, Crystal–liquid interfacial free energy and thermophysical properties of pure liquid Ti using electrostatic levitation: Hypercooling limit, specific heat, total hemispherical emissivity, density, and interfacial free energy, The Journal of Chemical Thermodynamics, 63 (2013) 1-6.
[98] J.J. Hoyt, A. Karma, M.A. Asta, D.Y. Sun, From atoms to dendrites, JOM, 56 (2004) 49-54.
[99] B. Echebarria, R. Folch, A. Karma, M. Plapp, Quantitative phase-field model of alloy solidification, Physical Review E, 70 (2004) 061604.
[100] T. Pinomaa, N. Provatas, Quantitative phase field modeling of solute trapping and continuous growth kinetics in quasi-rapid solidification, Acta Materialia, 168 (2019) 167-177.
[101] S. Ghosh, L. Ma, N. Ofori-Opoku, J.E. Guyer, On the primary spacing and microsegregation of cellular dendrites in laser deposited Ni–Nb alloys, Modelling and Simulation in Materials Science and Engineering, 25 (2017) 065002.
[102] S. Sahoo, K. Chou, Phase-field simulation of microstructure evolution of Ti–6Al–4V in electron beam additive manufacturing process, Additive Manufacturing, 9 (2016) 14-24.
[103] M.H. Burden, J.D. Hunt, Cellular and dendritic growth. II, Journal of Crystal Growth, 22 (1974) 109-116.